Applied Ocean Research 162 (2025) 104726



Contents lists available at ScienceDirect

Applied Ocean Research

journal homepage: www.elsevier.com/locate/apor



Research paper

The variability of wave-in-deck loading in random seas: a data-driven approach

Chong Huo, Li Ma, Ioannis Karmpadakis *

Department of Civil and Environmental Engineering, Imperial College London, South Kensington Campus, London SW7 2AZ, UK

ARTICLE INFO

Keywords:
Extreme waves
Wave-in-deck
Data-driven

ABSTRACT

This study investigates wave-in-deck (WID) loading in random sea-states. These are among the most severe forces experienced by offshore structures and a critical factor in assessing their reliability. Earlier research demonstrated that WID loading is fundamentally determined by a momentum-exchange process governed by the properties of both the incident wave and the topside structure. However, observations made in quasi-deterministic (QD) focused waves did not fully explain the larger variability (uncertainties) of the loading observed in realistic random sea-states, which is an essential consideration for a full reliability analysis.

To address this gap, WID loading measurements were conducted across a broad range of random sea-states using a realistic model topside structure. The resulting large dataset was analysed using a data-driven methodology to identify the key factors influencing maximum WID loads. The findings confirm the significance of incident wave momentum. Importantly, the results highlight the increased influence of the spatial and temporal evolution of the incident waves relative to the topside. It is evident that the more diverse forms of wave evolution in random seas account for the increased variability in WID loads. This was further demonstrated through a novel data-driven model, which accurately reproduced short-term WID loading distributions using only a small set of inputs derived from free-field wave data. The general applicability of the model across different sea-states without re-training allows more efficient reliability assessments, significantly reducing the need for extensive model testing.

1. Introduction

On offshore platforms, wave-in-deck (WID) loading occurs when an incident wave crest exceeds the topmost part of the sub-structure, directly impacting the topside (or deck structure) and the utilities within. In such cases, the level of inundation, $\Delta\eta$, becomes positive, such that

$$\Delta\eta = \eta_c - h_d > 0, \tag{1}$$

where η_c is the incident wave crest elevation and h_d the elevation of the underside of the deck structure. The interaction between the high water particle velocities near the wave crest and the densely-packed topside, which houses equipment and utilities, makes it particularly vulnerable to concentrated forces during WID events. In addition, WID loading produces a significant overturning moment due to the force being applied at the topmost part of the structure. WID loading is therefore among the most critical loading events affecting offshore platforms, as it significantly increases the total applied load and exposes the structure to a heightened risk of both local and global failure. As a result, it is a major engineering concern, especially as part of a reliability analysis for the design and re-assessment of an offshore structure.

Compared to loading arising on the lower parts of the structure, such as on a jacket-type sub-structure, a distinguishing feature of wave-in-deck (WID) loading is its large variability, even for similar incident wave crest elevations (and consequently similar $\Delta\eta$, assuming h_d is constant). This effect has been demonstrated by Ma and Swan (2023b) through direct comparisons. The increased variability arises because WID is governed by the uppermost part of the wave, where nonlinear effects are most pronounced and accompanied by the highest level of uncertainty. Moreover, realistic design wave conditions are irregular, highly nonlinear, and directionally spread, further amplifying the uncertainties within the applied loads. Traditional design methods, such as those based upon regular wave theories (for example, DNV-GL, 2019 and API, 2014), often fail to adequately capture this variability (Ma and Swan, 2023b). However, addressing these uncertainties is crucial for reliability analyses, as they have a direct and significant influence on the accurate assessment of structural failure probabilities. Whilst many recent researches are focused on wave impact on deck structures

* Corresponding author.
E-mail addresses: chong.huo15@imperial.ac.uk (C. Huo), l.ma@imperial.ac.uk (L. Ma), i.karmpadakis@imperial.ac.uk (I. Karmpadakis).

https://doi.org/10.1016/j.apor.2025.104726
Received 7 April 2025; Received in revised form 29 June 2025; Accepted 28 July 2025
Available online 16 August 2025
0141-1187/© 2025 The Author(s). Published by Elsevier Ltd. This is an open access article under the CC BY license (http://creativecommons.org/licenses/by/4.0/).

(for example, Fei et al., 2024, Duong et al., 2024, Wu and Chang, 2024, Chuang et al., 2023, Zhou et al., 2023 and Wang et al., 2022), fewer studies are dedicated to explaining the variability of WID loads arising in random seas.

To improve understanding in this area, previous studies (Ma and Swan, 2020a, 2023a) have explored wave-in-deck (WID) loading under quasi-deterministic (QD) focused wave conditions, providing insights into the momentum transfer mechanisms driving the loading. These studies demonstrated that factors such as the properties of the incident wave, its evolution, direction of approach, and topside porosity significantly influence the rate of momentum transfer from the incident wave crest to the topside structure, and consequently the magnitude of WID loads. Notably, given the intermittent nature of the wave-structure interaction, the applied WID loading was accurately predicted using an efficient momentum-flux model, which estimates momentum intake based on free-field incident wave conditions (Ma and Swan, 2020b). Nevertheless, random seas introduce additional complexities due to the broader range of wave forms that arise and interactions that are not fully captured by QD focused waves. This has been widely confirmed by previous researches such as Karmpadakis et al. (2019) and Toffoli et al. (2024). Indeed, WID loads arising in random seas have been observed to exhibit much larger variability (Ma, 2017) that could not be explained by the variations in the deterministic wave events employed in previous studies. Not only the general applicability of this observation needs confirmation, an explanation to this increased variability requires further investigation in a wide range of random sea-states. This paper addresses this gap by analysing WID loading arising in random seas, focusing on the key factors contributing to its variability. This is achieved by:

(a) Experimentally generating a large dataset comprising both the *free-field* (without topside) incident waves and the corresponding WID loading data, undertaken in a broad range of random sea-states.
(b) Identifying and analysing the key incident wave properties that determine the magnitude of WID loading and understanding their physical significance. This is achieved by evaluating these properties based on the surface elevation measurements and analysing the dataset using a data-driven approach. Specifically, Artificial Neural Network (ANN) models are adopted to systematically test a wide range of parameters that may influence the measured loads, utilising the ANN's efficiency and versatility in handling large datasets.
(c) Demonstrating the effectiveness of this analysis by reproducing both the expected magnitude and variability of WID loading observed in the experimental data. This is achieved using a refined ANN model and only a small number of free-field wave properties identified in (b).

In this study, the focus is on the horizontal component of WID loading in the mean wave direction, as it represents the largest load component most associated with global structural failure. As such, it is the primary concern in reliability analyses, particularly for typical topside structures of fixed platforms that incorporate relatively open and/or grated decks. However, the proposed methodology can be extended to any other force components, such as the vertical WID loading, as long as the loading remains momentum-driven.

Relevant technical background is provided in Section 2, followed by an introduction of the experimental programme in Section 3. The paper continues in Section 4 identifying and estimating the key incident wave properties that best define the maximum horizontal WID loading, F_x, as well as applying a data-driven methodology. The key findings are reported in Section 5, discussing the quantitative relationships between WID loading and the identified wave properties. Section 6 confirms the findings by reproducing the measured WID forces using a data-driven model with the identified wave properties as input. The paper concludes in Section 7, highlighting the practical implications of its contributions.

2. Background

Whilst a reliability assessment seeks to define the long-term probability of failure of a structure across many storms over the required return period, the probability of occurrence (or exceedance) of a particular wave or loading event is often first defined within individual storms, or sea-states. The probability distribution of a variable, such as the maximum crest height or loading caused by individual waves, that arises within the same sea-state is known as a short-term distribution. Examples of commonly used short-term crest height distributions can be found in Forristall (2000), Tayfun and Fedele (2007), Karmpadakis and Swan (2022) for crest heights and Tayfun (1981), Boccotti (1989), Karmpadakis et al. (2020, 2022) for wave heights. These are then convoluted with the long-term probability distribution of the sea-states to produce the long-term distribution (e.g. Forristall, 2008).

Traditionally, short-term distributions are generated using long time-domain random simulations, which experimentally model the conditions of specific sea-state(s) over a prolonged period of time. As such, they are both expensive and time-consuming. An alternative is to adopt quasi-deterministic (QD) focused waves following the *NewWave* design methodology (Tromans et al., 1991) and the theories of Lindgren (1970), Boccotti (1989) and Phillips et al. (1993). Derived using the auto-correlation function of the underlying wave frequency spectrum, these QD focused waves represent the expected shape of the largest waves arising in a (Gaussian) sea-state (Karmpadakis and Swan, 2020). While the underlying theory has been derived on the basis of linear wave theory, it has been adapted to produce nonlinear and breaking waves (Baldock et al., 1996; Johannessen and Swan, 2003; Gibbs and Taylor, 2005; Arena et al., 2008; Adcock et al., 2012; McAllister et al., 2018; Seiffert and Ducrozet, 2018; Alberello et al., 2018).

Adopting this approach, Ma and Swan (2020a, 2023a) studied the relationship between F_x and properties of the incident wave. They examined the changes in the (experimentally measured) WID loading as a result of variations in the incident wave properties, including their evolution and direction of propagation relative to the topside structure. It was found that WID loading is primarily a momentum-driven process. It follows that the applied WID loading must be closely related to the total momentum carried by the part of the wave that enters the topside. As such F_x is, in turn, determined by two factors: the volume of water that enters the topside and the associated water particle kinematics. Whilst the former dominates in non-breaking waves, the latter becomes the driving factor with the onset of wave breaking, especially wave over-turning. A separate study (Ma and Swan, 2020b) provided a model based upon a momentum formulation. Due to the fundamental assumptions of the model being very close to the physical reality of the WID loading process, the applied WID loading time-histories were accurately predicted without the requirement of any empirically calibrated coefficients (Millar et al., 2025).

From the studies mentioned above, it was clear that wave crest elevation alone does not determine the magnitude of the applied loads. Indeed, even with constant h_d and η_c, the load exhibited significant variability across different focused wave cases. However, these do not seem to explain the significantly larger variability observed in random seas. This is clearly demonstrated in Fig. 1(a), comparing WID loading measured in random and focused waves; the latter data provided by Ma and Swan (2020a). In both cases, the maximum WID loading, F_x, is plotted against the incident wave crest elevation that caused the loading event, defined as the maximum crest elevation arising over the entire plan area of the structure, η_c^A. These relate to the data labelled as 'corresponding' within the figure. In contrast, the 'QQ-plot' (short for quantile-to-quantile plot) is produced using the ranked values of F_x and η_c^A. This representation is widely adopted to describe short-term loading statistics (Heidman and Weaver, 1992), by associating crest heights and forces of the same exceedance probabilities. This helps to define the exceedance probability of the forces from given crest elevations, and provides a representative value through the 'corresponding' data.

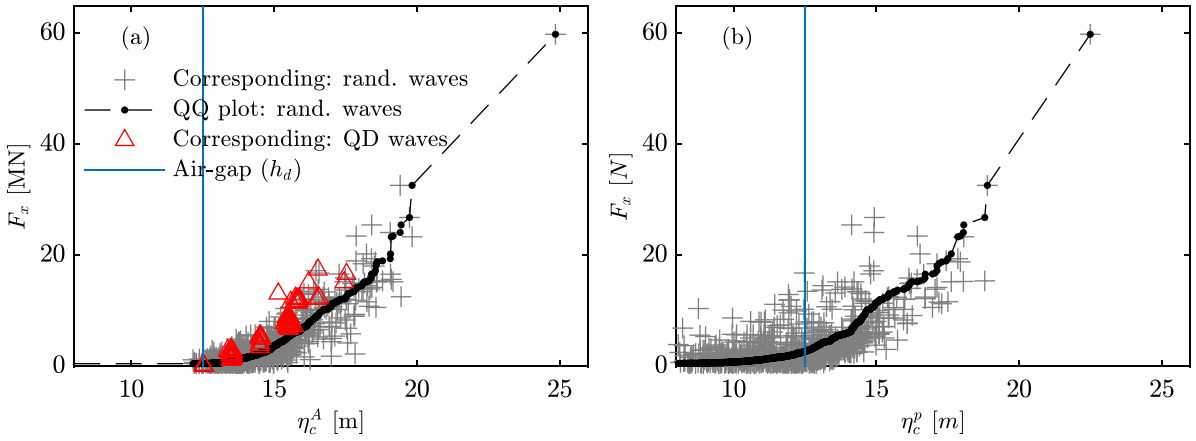


Fig. 1. The maximum measured WID force, F_x, plotted against the maximum incident crest elevation measured (a) over the entire plan area of the deck structure (η_c^A) and (b) at a fixed point in space, η_c^P, at the geometric centre of the structure; (b) area maximum crest height, η_c^A, within the area underneath the topside.

Within Fig. 1(a), the data relating to QD focused waves involve an extensive variation in the incident wave properties. These include, but are not limited to, the crest height, the directional spread and the underlying spectral shape. Despite this, the variability in the corresponding F_x values remains relatively limited. In contrast, F_x arising from random waves exhibit a much larger variability at any given η_c^A. For example, at $\eta_c^A = 16$ m, the F_x values from random waves could approximately range from 1 to 10 MN, whilst the F_x from QD waves is narrowly concentrated at around 8 MN. Understanding the physical mechanisms that drive this increase in the variability is key to the present paper, as it is directly relevant to the exceedance probability of the applied loading and therefore defines the probability of failure of the structure. Moreover, it should be noted that at a given level of η_c^A, the QD waves, on average, give rise to larger WID loads compared to those arising in random seas. Both points are investigated within the current paper.

Finally, Fig. 1(b) presents an alternative version of the WID loading measured in random waves. In this case, a more conventional measure of the incident wave crest elevation was adopted; the latter obtained at a single point at the centre of the structure (η_c^P). Comparing the two sub-plots of Fig. 1, three points are relevant:

(i) On Fig. 1(a), where η_c^A is adopted, all WID loads are shown to be caused by incident wave crests exceeding h_d, or the air-gap. This is expected but not the case in Fig. 1(b) when η_c^P is adopted.
(ii) F_x appears to correlate better with η_c^A than with η_c^P, with substantially reduced variability about the QQ-plot.
(iii) The explanation for both points lie in the fact that incident wave crests evolve over the plan area of the deck structure; the individual maxima at a single (arbitrarily) chosen point not being representative of the overall problem.

For these reasons, the level of inundation, or $\Delta\eta$, is best defined in terms of η_c^A in the context of WID loading. As such, this more appropriate definition of the incident wave crest elevation will be adopted in QQ-plots henceforth.

3. Experimental programme

The experiment was undertaken within the deep water basin in the Hydrodynamics Laboratory at Imperial College London. Both the free-surface elevations of the (free-field) incident waves, and the applied WID loading, are measured. Initially, the free-field incident waves are generated and measured using an array of wave gauges (WG) (Section 3.1). Once the free-surface measurements are complete, the wave gauges are replaced with a model topside structure (Section 3.3). The same wave conditions are then re-generated to capture the corresponding loading data. The success of this approach requires a fully-repeatable wave generation. The latter has been thoroughly validated by Latheef and Swan (2013) and Karmpadakis et al. (2019) with experiments conducted in the same facility. To ensure the practical relevance of the dataset, all the present experiments have been conducted by maintaining a Froude number (Fr) similarity between the laboratory and prototype scales, with a length-scale of $l_s = 1 : 100$ and associated time-scale of $t_s = 1 : 10$.

3.1. Wave generation and measurement

Fig. 2(a) and 2(b) provide a picture and a schematic of the wave basin, respectively. The facility has a working area of 20 m × 10 m, with a variable water depth being set to $d = 1.25$ m. A set of 56 independently controlled flap-type wave paddles are installed along one of the longer sides, and a perforated beach on the opposite side to minimise reflections. Glass panels are installed on the other two sides (along the x-axis) for maximum visual access. Each paddle, 0.35 m in width, is bottom hinged at 0.7 m below the still water level (SWL) and connected to adjacent paddles by soft and impermeable nylon membranes to prevent water leakage and allow the independent movement of the paddles. The wave generation system is digitally controlled and is capable of accurate wave generation within a frequency range of $0.3\,\text{Hz} \le f \le 3\,\text{Hz}$. Waves can be generated at oblique angles between up to 45° relative to the paddles. The paddles are controlled with a force-feedback system with active absorption capabilities, ensuring the correct generation of all underlying linear wave components without a build-up of wave energy within the basin (Spinneken and Swan, 2009a,b). Indeed, combining the active (paddles) and passive (beach) absorption minimises any unwanted wave reflection, which is typically below 5% (Masterton and Swan, 2008). For further evidence of the accurate generation of the desired incident wave spectra and the high quality of the waves generated, the reader is referred to previous studies such as Latheef and Swan (2013) and Karmpadakis et al. (2019).

Fig. 2(b) also provides a schematic of the resistance-type, tensioned-wire wave gauge (WG) array. A long row of 15 wave gauges with variable spacing ($\Delta x = 0.1$ m close to the structure and $\Delta x = 0.2$ m further away from the structure) is placed along the centre-line of the basin and allows for improved recording of the wave evolution. In addition, a square section of 49 equi-spaced ($\Delta x = \Delta y = 0.1$ m) wave gauges is positioned in the middle of the tank to provide better coverage over the footprint of the topside and a finer spatial resolution. Fig. 3(c) provides a detailed view of this latter part. The wave gauges are calibrated on a daily basis (to an error of within 1%) and record the surface elevation at 128 Hz, providing a high temporal resolution. The position of the model topside which was used for the second phase of the experiment is also superimposed on Fig. 2(b).

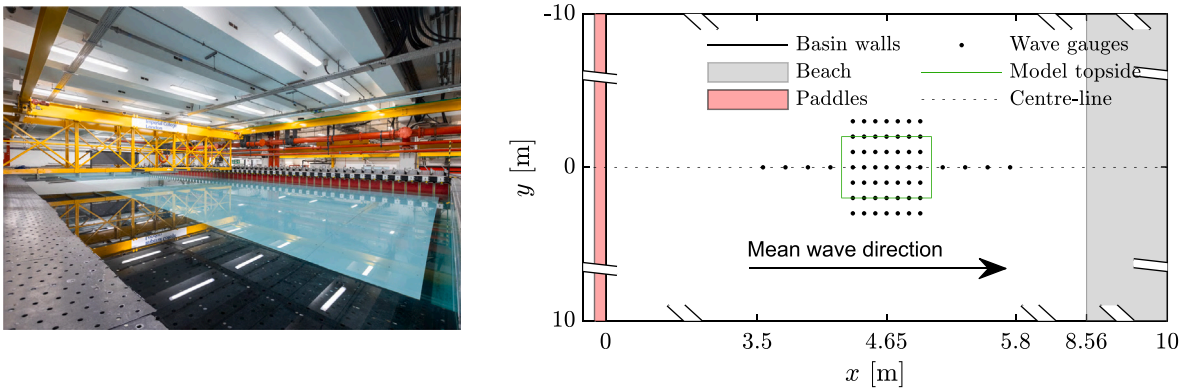


Fig. 2. (a) A picture of the deep water basin in the Hydrodynamics Laboratory at Imperial College London. (b) Schematic showing a plan view of the wave basin, the layout of the wave gauges and the position of the model topside.

Table 1
Sea-states within the present study. All values are expressed in prototype scale.

ID	H_s [m]	T_p [s]	γ	σ_θ [°]	$S_p = \frac{2\pi H_s}{gT_p^2}$	$k_p d$	Duration [h]	No. of WID events
SS1	15	16	2.5	20	0.038	2.03	230	1400
SS2	12	16	2.5	20	0.030	2.03	110	50
SS3	15	16	5	20	0.038	2.03	110	550
SS4	15	16	1	20	0.038	2.03	110	750
SS5	15	14	2.5	20	0.049	2.60	110	1200
SS6	15	16	2.5	10	0.038	2.03	110	800
SS7	15	16	2.5	0	0.038	2.03	110	800
SS8	17.5	16	2.5	20	0.044	2.03	110	2100

3.2. Wave conditions

All random sea-states within this work are based upon a JONSWAP frequency spectrum (Hasselmann et al., 1973) given by:

$$S_{\eta\eta}(f) = \frac{\alpha g^2}{(2\pi)^4 f^5} \exp\left[-\frac{5}{4}\left(\frac{f}{f_p}\right)^{-4}\right]\gamma^{G(f)}, \tag{2}$$

$$\text{where } G(f) = \exp\left[-\frac{1}{2}\left(\frac{f/f_p - 1}{\sigma}\right)^2\right], \tag{3}$$

γ is the peak enhancement factor, α the energy scale factor, f_p the spectral peak frequency and $g = 9.81\,\text{ms}^{-2}$ the gravitational acceleration. The peak width parameter is defined as $\sigma = 0.07$ for $f \leq f_p$ and $\sigma = 0.09$ for $f > f_p$ (Holthuijsen, 2007). The (frequency-independent) directional spreading function $D(\theta)$ is defined as a wrapped normal distribution:

$$D(\theta) = \frac{A}{\sigma_\theta}\exp\left(\frac{-\theta^2}{2\sigma_\theta^2}\right), \tag{4}$$

where A is a normalising parameter and θ represents the propagation angles of individual wave harmonics relative to the mean wave direction. The directional spread is, thus, controlled by the standard deviation of the normal distribution, σ_θ. The two–dimensional wave spectrum, $E(f,\theta)$, is then given by:

$$E(f,\theta) = S_{\eta\eta}(f)D(\theta), \tag{5}$$

Using Eq. (5), the present study defines a wide range of sea-states using four parameters: the significant wave height (H_s), the spectral peak period (T_p), the peak enhancement factor (γ) and the directional spreading (σ_θ). These are summarised in Table 1, where SS1 is the base case with $H_s = 15\,\text{m}$, $T_p = 16\,\text{s}$, $\gamma = 2.5$ and $\sigma_\theta = 20°$.

The duration of each random realisation is $T_d = 2048\,\text{s}$. With a constant frequency spacing of $df = 1/T_d$, each wave frequency spectrum is defined by at least 3000 Fourier components, which is sufficient to ensure appropriate representation of sea-state randomness (Karmpadakis, 2019). The data within the table and for the remainder of the paper are all expressed in prototype scale, unless otherwise stated. Using SS1 as the 'central case', the four sea-state parameters are systematically varied to define the other sea-states. It should be noted that all sea-states are associated with an effective water depth equal to or larger than $k_p d = 2.03$, where k_p is the wave number associated with T_p, representing intermediate to deep water conditions. The steepness of these sea-states is such that they represent realistic design conditions, and are substantially affected by non-linear effects (Latheef and Swan, 2013; Karmpadakis et al., 2019).

3.3. Topside model and load measurement

A realistic topside model is considered within the present study. The internal arrangements of this structure is illustrated in Fig. 3, which presents views from both above and below. The deck is constructed with open grating similar to a wide range of offshore platforms, allowing water to enter or exit the topside through the floor. Fig. 3(c) provides a schematic showing the alignment of the topside with the wave gauge array and the axis of the wave basin, with the tanks/containers facing the incident waves. The elevation of the topside is adjusted to maintain an air-gap of $h_d = 12.5\,\text{m}$. A jacket sub-structure is not included. As such, the incident wave condition is undisturbed until it reaches the topside. This is consistent with the 'slender-body' assumption for typical jacket structures where the incident wave is virtually undisturbed by the sub-structure, as well as allowing the present study to focus on WID loading. Whilst this may exclude the situations where the incident wave conditions are amplified due to the presence of, for example, densely-packed riser arrays, it is outside the scope of the present investigation. The loading arising on the topside is measured using a bespoke 6-degree-of-freedom load cell, sampling at 12 kHz. For a detailed explanation of the model topside, the load measurement system, along with a full validation of its measurements, quality control and data post-processing, the readers are referred to Ma and Swan (2020a, 2023a). It should be noted that although the data

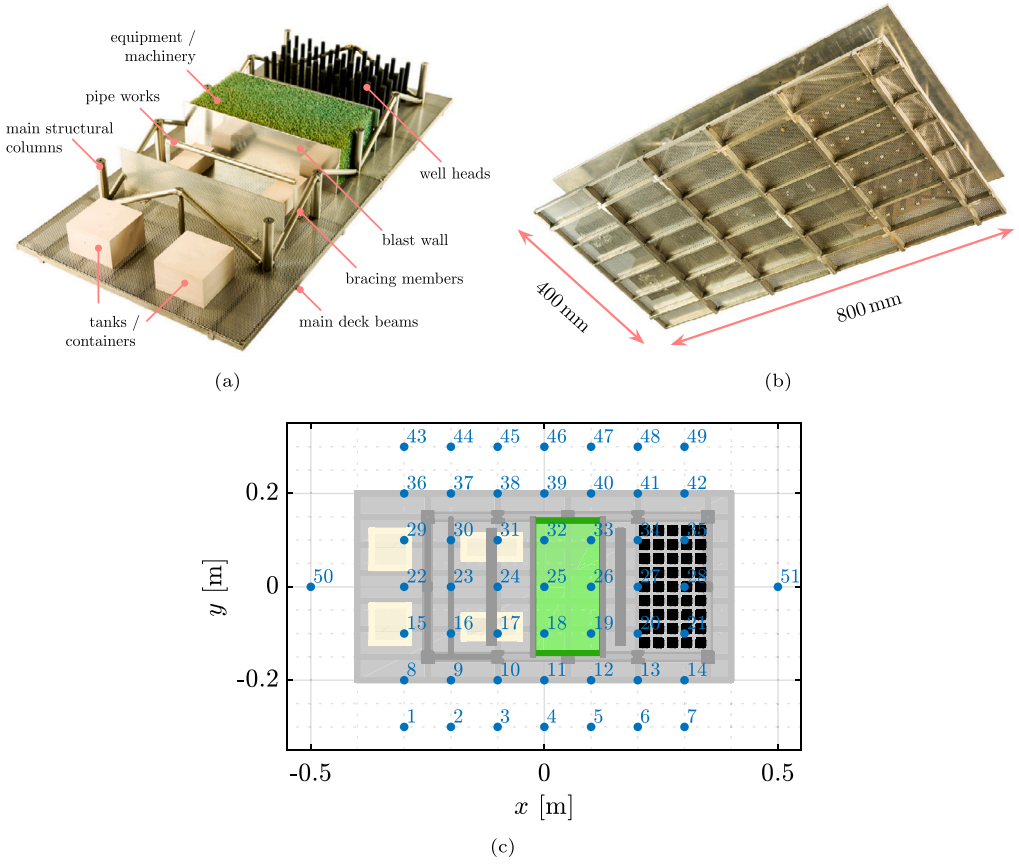


Fig. 3. Dimensioned and annotated photographs of the realistic model topside, viewed (a) from above and (b) below, as provided by Ma and Swan (2023a). Subplot (c) is a schematic showing the plan view of the topside in relation to the central part of the wave gauge (WG) array superimposed. The axes are consistent with those given in Fig. 2(b). The blue dots indicate the positions of the wave gauges. Dimensions are provided in laboratory scale.

used for the present study relates to a single topside structure with fixed elevation and orientation, the analysis and the results will provide insights that are generally applicable to other structures.

4. Data and analysis approach

Once the data are collected, analyses are performed on a wave-by-wave basis. First, WID loading events are identified from the horizontal force time-histories, $F_x(t)$. The corresponding wave event, with data from all wave gauges, is then isolated from the incident free-surface measurements. This provides a complete space–time record of the undisturbed wave evolution, $\eta(x, y, t)$, over the approximate footprint of the topside structure. The maximum values observed in $\eta(x, y, t)$ and $F_x(t)$ yield the maximum wave crest elevation (η_c^A) and the maximum WID loading (F_x), respectively. It is exactly this analysis that produced the random wave data presented in Fig. 1(a). Second, $\eta(x, y, t)$ is further processed to generate a list of key parameters (see Section 4.1 and Table 2), relating the incident wave evolution and loading process. These are used alongside estimates of wave kinematics (Section 4.2) to derive an artificial neural network model (see Section 4.3). The latter is employed to explore the correlation between these key parameters and the corresponding WID loading (F_x), utilising its capability to efficiently analyse large datasets. These steps are discussed in more detail in the following sections.

4.1. Parametrising a free-field incident wave profile

For QD focused waves, the maximum WID loading, F_x, is primarily driven by two parameters, the maximum volume of water that enters the deck ($V_{\max}$), and the associated maximum horizontal water particle kinematics ($u_{\max}$). The large variability of incident wave forms observed in random waves requires a few more parameters to be considered. This is to ensure that the unique shape and evolution of each incident wave event are adequately represented in studying their correlation with F_x. A full list of the parameters considered herein is provided in Table 2 alongside their description. These include common zero-crossing quantities such as wave crests, η_c, heights, H, and periods, T, derived using zero-crossing analyses. The various definitions of these quantities are illustrated in Fig. 4(a) using an example random wave recorded on a single wave gauge, whilst Fig. 4(b) provides an additional illustration for the definition of $V_{\max}$. In addition, several derived variables such as the local asymmetry measures (e.g. α, β) and steepnesses (e.g. S_{t1}, S_{t2}) are also used with the aim to better describe the incident wave characteristics.

Finally, the local spectrum is used to derive representative individual wave properties that could be important in the context of WID loading. These include, for example, the focal quality (Q) (Johannessen and Swan, 2003), mean spectral frequency ($\bar{f}$), spectral bandwidth (ν) and directional spreading (S) (Donelan et al., 1996) of individual waves. This last set of parameters requires the definition of a local spectrum for individual waves. While Fourier decomposition is typical for the analysis of entire sea-states, such short signals require a wavelet-type analysis (see, e.g. Powers et al., 1998; Krogstad et al., 2006; Ma et al., 2010). A variant of this, the Stockwell Transform (Stockwell et al., 1996), is adopted in the present study to obtain the local spectrum. This is defined as:

$$S_l(\tau, f) = \int_{-\infty}^{\infty} h(t) \frac{|f|}{\sqrt{2\pi}} e^{-\frac{(\tau-t)^2 f^2}{2}} e^{-i2\pi f t} dt, \tag{6}$$

where S_l is the local spectrum, τ the time, f the frequency and $h(t)$ the time-series signal. Similar to the Fourier spectrum, the local spectrum

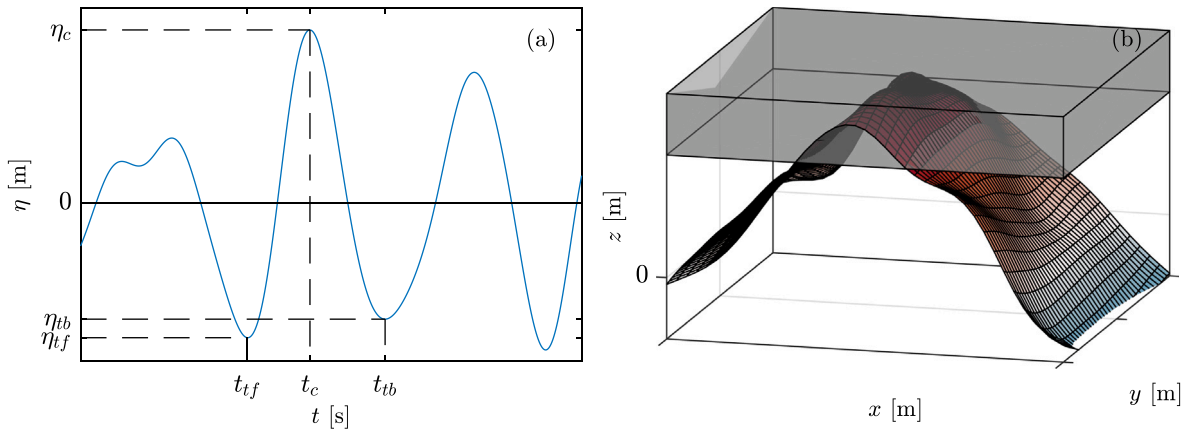


Fig. 4. (a) An example of a random wave record measured on a single wave gauge, showing the definition of the notation adopted within the present study. (b) An example of an incident wave crest entering the space occupied by a deck structure. In this case $V_{\max}$ is defined as the integral volume of the part of the wave that is within the deck; the latter represented by the grey box.

Table 2
A list of key parameterisation of the incident wave profile, $\eta(x, y, t)$.

Parameter	Definition
$V_{\max}$	The maximum volume of water that would enter the topside structure. This value is computed as the spatial integral of the free-field surface elevation that is within the structure, illustrated in Fig. 4(b) and further explained in the captions.
η_c	The wave crest height measured at a single wave gauge.
H	The wave height defined with an up-crossing analysis, $H = \eta_c - \eta_{tb}$.
η_c/H	The wave crest-to-height ratio as a measure of second-order contributions.
$\beta = \eta_{tf}/\eta_{tb}$	The front–back trough ratio which provides an indication for horizontal wave asymmetry. Lindgren and Prevosto (2021) reported a link between such an asymmetry and the orientation of particle orbits.
$\alpha = T_{tc}/T_{ct}$	Alternative measure of the front–back wave asymmetry using wave periods: $T_{tc} = t_c - t_{tf}$ and $T_{ct} = t_{tb} - t_c$.
$S_{t1} = \eta_c k_{tt}$	Crest steepness associated with the trough-to-trough wave number, k_{tt}, related to the period T_{tt} through the linear dispersion equation.
$S_{t2} = \eta_c k_{tc}$	Front-face crest steepness associated with the trough-to-crest wave number k_{tc} calculated using $2T_{tc}$ (Stansberg, 2020).
$S_{t3} = \eta_c k_{ct}$	Back-face crest steepness defined as above, but using k_{ct}.
$Q = \frac{\sum_i a_i \cos(\phi_i)}{\sum_i a_i}$	Focal quality of a wave (Johannessen and Swan, 2003), defined by the amplitude, a_i, and relative phasing, ϕ_i, of the ith frequency component in the local spectrum Eq. (6).
$\Theta = \sum_i a_i \theta_i / \sum_i a_i$	Weighted mean (individual) wave propagation direction calculated using the direction of travel of the ith spectral component, θ_i, following the method of Donelan et al. (1996) and the local spectrum.
$S = \frac{\sum_i a_i \cos(\theta_i - \Theta)}{\sum_i a_i}$	Directional spreading of individual waves calculated as above.
$\bar{f} = m_1/m_0$,	Spectral mean frequency using the first two spectral moments (m_0, m_1) of the local spectrum.
$\nu = \sqrt{\frac{m_0 m_2}{m_1^2} - 1}$	Spectral bandwidth calculated using m_0, m_1 and m_2 from the local spectrum.

can be used to derive spectral moments, m_n, as

$$m_n = \int_{-\infty}^{\infty} f^n S_l(\tau, f) df, \tag{7}$$

where n denotes the order of the moment.

4.2. Water particle kinematics

Considering the contribution of the horizontal water particle velocity, u on F_x, an effort is made to best approximate it using free-surface quantities. This is because measuring wave kinematics in both experimental and field settings is considerably more difficult and less accurate than surface elevations. For this reason, we employ the method proposed by Grue et al. (2003) to estimate u as:

$$u = \epsilon \sqrt{g/k} e^{kz}, \tag{8}$$

where g is the gravitational acceleration, k the wave number, z the vertical coordinate measuring upwards from the still water level and ϵ the wave steepness which is, in turn, only dependent on η_c and k. As such, an approximation of the horizontal kinematics at any given elevation can be entirely defined using quantities derived from the free-surface measurements.

Whilst η_c can be directly taken from the measured surface elevation, an ambiguity arises in the estimation of k, which is related to the wave period T through the dispersion equation. However, several definitions (e.g., trough-to-trough, crest-to-trough) can be used for describing wave period of irregular (random) waves (Guedes Soares et al., 2004). Upon testing the available variants, the present work proposes a local spectral mean frequency ($\bar{f}$), defined in Table 2, as a measure of the local wave frequency of individual random waves. The local wave period is then calculated as $T = 1/\bar{f}$.

The appropriateness of Eq. (8), applied with the above-mentioned definition of the wave number k through $\bar{f}$, is demonstrated in Fig. 5. Sub-plot (a) compares Grue et al.'s (2003) estimation, $\hat{u}_{\max}$, with the maximum horizontal water particle velocity under the wave crest ($u_{\max}$) calculated using a second-order random wave theory (Sharma and Dean, 1981). The comparison is carried out for the largest waves

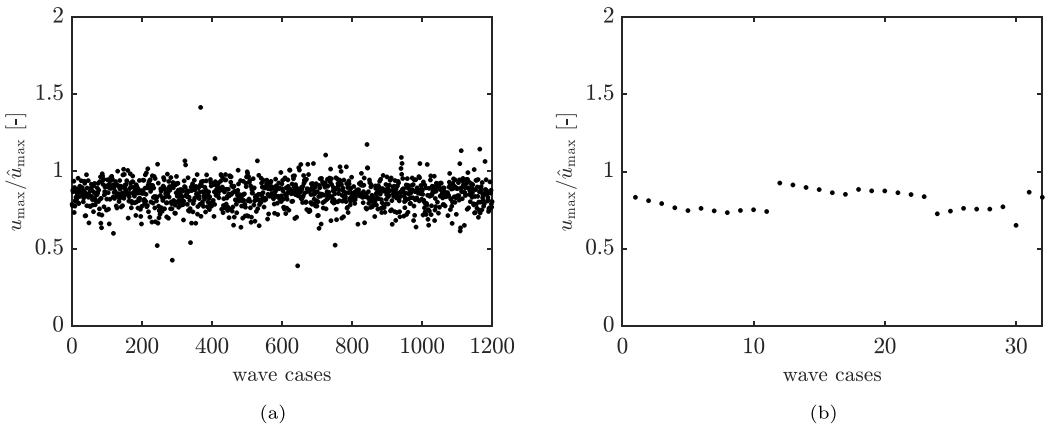


Fig. 5. A comparison between the estimated maximum horizontal water particle velocities following Grue et al. (2003) ($\hat{u}_{max}$) and calculations using a (a) second-order calculation following Sharma and Dean (1981) and (b) fully-nonlinear Boundary Element Method (BEM) (Hague and Swan, 2009). The data presented in (a) are based upon sea-state SS1 and those in (b) on QD waves by Ma and Swan (2020a).

arising from the random sea-state SS1. In Fig. 5(a), the ratio $u_{max}/\hat{u}_{max}$ is centred around 0.85, with a small standard deviation of 0.08, indicating the success of this approach. Putting this into context, if the trough-to-trough period was adopted as the local wave period instead of $1/\bar{f}$, this standard deviation would increase to 0.19. In fact, the proposed method outperforms any other wave periods based on a zero-crossing analysis. This arises because all other measures of the local wave period are significantly affected by the shape of the adjacent troughs. Therefore, it does not effectively capture information about the wave crest itself. In contrast, the local mean wave frequency ($\bar{f}$) is determined directly at the wave crest, making it a more appropriate measure.

Furthermore, the proposed method is also compared to fully-nonlinear calculations in Fig. 5(b). In this case, the calculations are based upon a simulation using the Boundary Element Method (BEM) (Hague and Swan, 2009), modelling the QD focused wave cases adopted by Ma and Swan (2020a). Once again, the ratio $u_{max}/\hat{u}_{max}$ clusters tightly around 0.8 with a standard deviation of 0.06. In reviewing these results, it should be noted that Alberello et al. (2018) previously reported an under-estimation of velocities at the wave crest by Grue et al.'s (2003) method. Despite some differences in the implementation of the method, it is accepted that large uncertainties arise in the estimation of the wave velocity at the crest. Ideally, the effects of this estimation uncertainty would be rigorously quantified by examining the statistical relationship between $\hat{u}_{max}$ and u_{max}. However, this is challenging within the current study (and any random wave study) due to the limited availability of u_{max} data. Nevertheless, considering Fig. 5 as a whole, $\hat{u}_{max}$ appears to provide a consistent estimate of u_{max} which is sufficient to support the analysis that follows - especially considering that the data-driven part of the methodology is set to identify and incorporate any potential bias in estimation methods.

4.3. A data-driven approach to data analysis

The analysis of the correlation between the variables listed in Table 2 and F_x is conducted using an artificial neural network (ANN), otherwise known as the Multi-Layer Perceptron (Hastie et al., 2009). It is one of the simplest and most fundamental machine learning models. An ANN consists of an input layer, one or more hidden layers and an output layer. Each layer consists of a set of nodes (or neurons). Information starts from the input layer, travels through the hidden layers and finally arrives at the output layer. With each neuron connected to all neurons in adjacent layers, they form a feed-forward and fully-connected structure.

While neurons in the input layer hold the input/independent variables of the model, each neuron in the (intermediate) hidden layers performs two types of transformations. The first is a linear transformation defined as:

$$z = \beta_0 + \beta_1 a_1 + \beta_2 a_2 + \cdots + \beta_n a_n, \tag{9}$$

where β_i is the weight, a_i the value from the ith neuron from the previous layer and n the number of neurons in the previous layer. This linear transformation is followed by a nonlinear one, which is a predefined *activation function*. For this step the present study adopts the ReLU function:

$$\mathrm{ReLU}(z) = \max(0, z). \tag{10}$$

Finally, neurons in the output layer perform a further linear transformation (Eq. (9)) to generate the final output. The power of this model lies in its universality; even a network with just one hidden layer can approximate any continuous function with enough neurons (Hornik et al., 1989).

Within the present study the structure of the ANN model, specifically the number of hidden layers and the number of neurons in each hidden layer, is optimised following a grid search approach. The chosen structure represents the best prediction accuracy during a 5-fold cross-validation. For example, the initial ANN model employs a large input layer consisting of 482 nodes representing the free-surface parameters (see Section 5.1) and a single-node output layer representing F_x. Between these, three hidden layers are used, with the number of nodes gradually reducing to 300, 30, and 9, respectively.

Training the ANN involves optimising the β coefficients in the network to minimise a loss function, which quantifies the overall discrepancy between the predicted and known output values in a certain dataset; the latter is referred to as the training set. The back-propagation algorithm (Bishop, 1995) is traditionally used for training, which calculates the partial derivatives of the loss function with respect to each β coefficient using the chain rule. These partial derivatives guide an iterative adjustment process of each coefficient, reducing the loss function step-by-step until it reaches a minimum. In this study, a Limited-memory Broyden–Fletcher–Goldfarb–Shanno (L-BFGS) optimisation algorithm (Nocedal and Wright, 2006) is used for the training of the ANN model. The stopping criteria for training relies solely on the convergence of the L-BFGS optimiser.

4.4. Importance of individual input variables

A preliminary assessment of the relative importance of the input variables is performed using the Mutual Information (MI) (Shannon, 1948), which is a measure of the 'amount of information' obtained for one variable by observing another variable. It is defined as:

$$\mathrm{MI} = \sum_{y\in Y}\sum_{x\in X} p(x,y)\log\left(\frac{p(x,y)}{p(x)p(y)}\right), \tag{11}$$

where X, Y are observations of the two random variables and p the probability distribution function. In the present study, Y is always F_x and X could be all independent variables (as defined in Table 2). The ones with larger MI values are likely to be more important.

In order to better determine which wave properties have unique (non-redundant) and important effects on F_x, a backward elimination method (Guyon and Elisseeff, 2003) is also adopted. Starting from all available independent variables, the least promising ones are progressively removed until a stop criterion is reached. In this case the MI analysis above provides a good indication on the order of parameter removal. The decision to whether a parameter is eliminated is based upon its level of redundancy; the latter is deduced from the change in the overall prediction accuracy of a model when it is removed from the inputs. In this research, the backward elimination is implemented with the ANN model, where the prediction accuracy is quantified using a root-mean-square error (RMSE) such that:

$$\mathrm{RMSE} = \sqrt{\frac{1}{n}\sum_{i=1}^{n}(F_{x,i} - \widehat{F_{x,i}})^2}, \tag{12}$$

where n is the number of observations, $F_{x,i}$ and $\widehat{F_{x,i}}$ are respectively the ith measurement and model output (or 'prediction'). A smaller RMSE suggests better agreement between the output and the measured data. Indeed, the RMSE is closely related to the loss function adopted for the ANN model and directly reflects the optimal performance of the model given a certain set of inputs. As such, a parameter is less important if its removal leads to an insignificant deterioration, or even improvement, of the prediction accuracy. For the present paper, the elimination process is summarised into the following steps:

(1) Investigate the relative importance of the parameters using MI.
(2) Remove the least promising independent variable from the input.
(3) Train a new ANN model with the remaining set of variables; evaluate its RMSE in a dataset that was not used for training.
(4) Accept the removal if the increase in RMSE is $\leq 10\%$ of the value given by the original model utilising all inputs, revert otherwise.
(5) Repeat steps (2) – (4) until attempts have been made to remove all independent variables.
(6) Reintroduce the removed variables one at a time and re-evaluate. Accept if the inclusion of this variable reduces the RMSE $> 10\%$.
(7) Attempt all combinations of the remaining variables and select the one combination with the best accuracy.

5. Results

5.1. Relative importance of key parameters

The present section discusses the results of the MI and backward elimination analyses as outlined in Section 4.3 above, undertaken using the parameters listed in Table 2 as inputs to the ANN model. In total, 14 parameters are listed. Whilst the computation of $V_{\max}$ requires data from all wave gauges, the other 13 can be calculated using data collected on any of the wave gauges depicted in Fig. 3(c). There are 35 wave gauges that overlap with the plan area of the topside model (WG8-WG42). Together with the wave gauges immediately upstream (WG50) and downstream (WG51) of the structure, data from 37 wave gauges are potentially the most relevant in terms of their influence on F_x. As such, the total number of independent variables is $1 + 13 \times 37 = 482$, which forms a high-dimensional parameter space.

Adopting an MI analysis, Fig. 6 demonstrates the relative importance of wave gauge locations with a contour plot of the average MI values of all properties in Table 2 on each wave gauge. The contour is plotted side-by-side with the plan view of the topside structure. Since both the plan view of the structure and the contour are symmetric about the centre-line (at $y = 0\,\mathrm{m}$), one half of each is presented. It is clear that the information gathered close to the centre of the topside ($x = y = 0\,\mathrm{m}$) is associated with the highest MI metric. This is where the deck is the most densely-packed (featuring a blast wall and equipment/machinery as shown in Fig. 3) and is therefore likely where the momentum is transferred at the highest rate, leading to increases in F_x. In addition, the MI values are generally higher on the upstream ($-x$) side of the structure, indicating the higher importance of the data gathered by the wave gauges in this region. This is expected as the upstream side is often the first point of contact for any undisturbed incident wave momentum.

From this initial analysis, it is clear that most of the 482 variables are expected to have a relatively small influence on F_x. The reason for this is three-fold:

(i) Measurements at adjacent wave gauges are highly correlated. The spacing between two neighbouring gauges is approximately 1 m in prototype scale. This is much smaller compared to the wave-length associated with the spectral peak period (approximately 400 m in the case of $T_p = 16\,\mathrm{s}$). The variation in the wave profile is generally continuous and is therefore relatively small between these adjacent gauges. Consequently, the inclusion of wave gauges that are immediately next to each other will likely provide little extra information.
(ii) Some parameters at certain locations are less important. For example, it is reasonable to expect that the wave steepness at the rear corner of the structure (WG42) to exert little influence on F_x.
(iii) The information incorporated by some wave properties are readily included in others. For instance, the front–back asymmetry (α) can potentially be inferred via the front-, central and back-face steepness values (S_{t2}, S_{t1} and S_{t3} respectively), calculated using different measures of the wave period.

Indeed, this final point is illustrated in Fig. 7, where the MI values for all parameters are presented in a ranked order. The MI values are averaged across all wave gauges (with the exception of $V_{\max}$ which utilises the data from all wave gauges to compute). Among all the parameters, the leading wave properties are $V_{\max}$ and η_c. However, whilst MI provides a good indication on which parameters are more influential on F_x, it can only be used as a preliminary measure. This is because there is no clear limit in the MI value below which an independent variable can be deemed as 'not important'. Moreover, MI cannot identify potential high correlation between independent variables. Specifically, two independent variables could both have high MI values but contain similar information. For instance, the wave height H is associated with a very high MI value, but also highly correlated to η_c, due to the fact that a wave with large η_c is statistically expected to have large H. When the effect of η_c is considered, the inclusion of H could be redundant.

To improve this and provide a more detailed insight, the backward elimination procedure was applied. In this case the steps outlined in Section 4.4 are performed for three rounds. Whilst all three rounds of backward elimination share exactly the same procedure, they focus on different groupings of the parameters. The first round addresses the wave gauges. In this round all the parameters associated with the same wave gauge are treated as one group and are removed or added simultaneously. Moreover, the data arising from symmetric pairs of wave gauges are also placed in one group, due to the fact that the topside is symmetric about the centre-line; the latter aligned with the mean wave direction. As such, information on wave gauges at symmetric locations must have identical importance.

Fig. 8 illustrates the change in RMSE when wave gauges are progressively removed without reverting. The vertical axis measures the model accuracy and the horizontal axis denotes the number of wave gauges that remains in the input. It is noted that the RMSE is normalised by the standard deviation of the measured data. In general, the RMSE increases as the number of wave gauges reduces. However, such increase is very

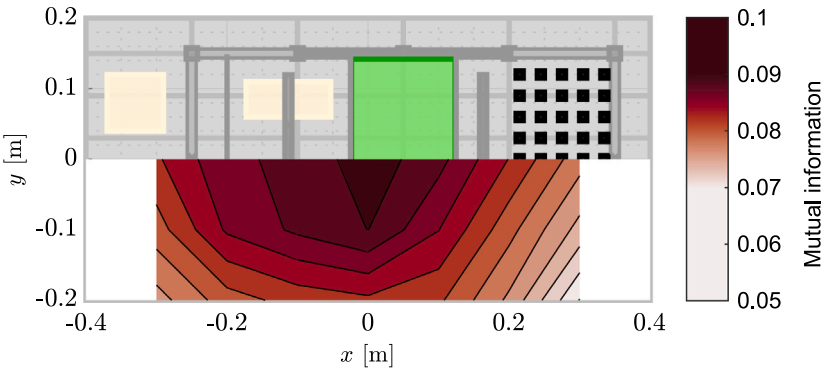


Fig. 6. A contour of the average MI values of all wave properties (from Table 2) on each wave gauge. The contour is plotted side-by-side with the plan view of the structure. Only half of the contour and half of the plan view are plotted, as their other halves are mirror images of the presented ones. Note that the contour plot does not cover the whole length of the topside due to the arrangement of the wave gauge array (see Fig. 3(c)). Dimensions are given in laboratory scale.

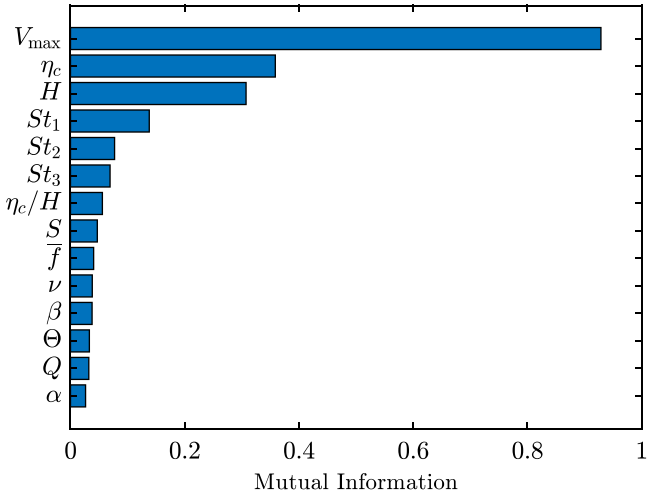


Fig. 7. Mutual Information of all free-surface parameters listed in Table 2. The values presented are the average across all wave gauges.

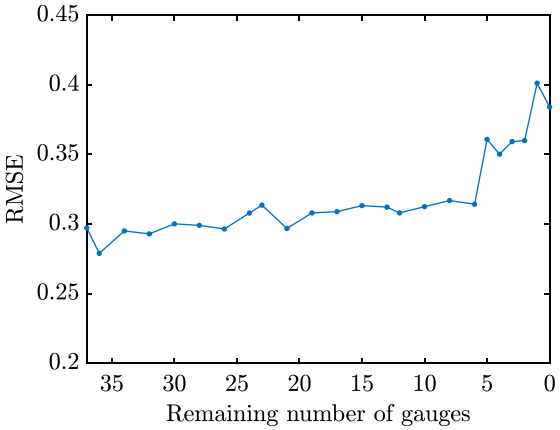


Fig. 8. The overall accuracy of an ANN model when data from each wave gauges are progressively removed (without reverting).

gradual until the last 6 gauges remain. This observation reflects the level of redundancy in the original set of inputs and confirms that data from most of the gauges can indeed be removed without significantly affecting the output. Interestingly, the change in RMSE becomes significantly larger when data from the last 6 remaining gauges are removed, indicating their significance. This is consistent with the fact that the order of removal is guided by the MI analysis discussed above, where the data relating to the least important wave gauges are removed first. When the remaining number of gauges reduces to zero, only V_{max} remains in the input. In this case, the model accuracy is much lower in comparison to the situation where the information on 6 wave gauges was included. Indeed, this provides the first evidence that at least some wave properties identified in Table 2 (other than V_{max}) have a significant influence on F_x.

Based upon the results of the first round of backward elimination, a second round is applied on the wave properties. Specifically, one wave parameter is removed altogether from the inputs at a time, irrespective of the wave gauge that acquired the data. With the remaining variables, a third round is carried out on individual parameters, treating each parameter measured on each wave gauge as a single entity. The final remaining independent variables are summarised in Table 3. Interestingly, only 11 wave properties remain, thus significantly reducing the parameter size from the original 482. The elimination process ensures that the removed variables are either relatively insignificant in terms of their effect on F_x, or their influence is already incorporated in other wave properties. As such, the final set represents an optimal balance between a small redundancy and a high level of influence on F_x.

Whilst the backward elimination results presented in Table 3 are consistent with those derived from the MI analysis, they provide additional clarity and insight. Taking each parameter in turn, V_{max}, calculated using the data collected from all wave gauges, is identified as a major factor in determining the magnitude of F_x. This is expected, as the mass-flux of water entering the deck structure plays a critical role in the rate of momentum transfer. Interestingly, η_c, measured at six wave gauge (WG) locations, also appears to be significant. Examining the locations of these wave gauges (see Fig. 3(c)) reveals their relevance to key elements of the topside structure, including:

(a) The front-centre (WG50, WG22) of the structure, where momentum transfer is typically at its maximum.
(b) The lateral extent of the structure (WG9, WG37), indicating how off-centred the incident wave crest is relative to the structure. This affects both the area of the structure being loaded and the associated water particle velocities.
(c) Locations before and after key structural elements that dissipate significant fluid momentum. For example, a fully-plated blast wall exists between WG25 and WG26.

Following on, the combination of η_c and $\bar{f}$ determines u_{max} (see Section 4.2), which is another critical factor in the momentum transfer process. Finally, Q, representing the 'goodness of focus' of individual wave components, appears significant at two points, spaced apart, along the centre-line of the structure. This indicates the persistence of V_{max} and u_{max} values as the waves propagate through the topside structure. Taken together, these findings suggest:

Table 3
Result of the backward elimination process, providing a set of the most important wave properties in determining the magnitude of F_x. The parameters are specified along with the wave gauges at which they are measured (see Fig. 3(c)).

Parameters	Wave gauges
V_{max}	all
η_c	50, 22, 25, 26, 9, 37
$\bar{f}$	50, 26
Q	50, 26

(1) V_{max} and u_{max} remain the primary drivers of F_x in random seas.
(2) The additional variability in F_x is related to the more varied spatial and temporal evolution of the incident wave crests.

All sea-states considered in this study yield similar results. This confirms that the applied WID loading is fundamentally determined by the rate of momentum transfer. Assuming the same topside structure, this momentum is governed by V_{max} and u_{max}. On a wave-by-wave basis, provided these terms are adequately defined, other less direct parameters such as directionality and spectral bandwidth, become less significant. Within the following sections, the effects of V_{max} and u_{max}, as well as trends in F_x resulting from variations in sea-state parameters, will be discussed in further detail.

5.2. Effects of the volume of water entering the topside

Fig. 9(a) illustrates the dependence of F_x on V_{max}. Utilising data from SS1, this figure provides a scatter plot of F_x against V_{max}. An Ordinary Least Squares (OLS) regression was performed to these data such that:

$$F_x = \beta_0 + \beta_1 V_{max} + \epsilon, \tag{13}$$

where β_0 and β_1 are the fitted constants and ϵ the residual. In this case the goodness of fit is assessed via the coefficient of determination, defined as:

$$R^2 = \frac{\sum_i (\widehat{F_{x,i}} - \bar{F}_x)^2}{\sum_i (F_{x,i} - \bar{F}_x)^2} \qquad (0 \le R^2 \le 1.0), \tag{14}$$

where i is the index of each data point, $\bar{F}_x$ the mean value of the measured loading and $\widehat{F_{x,i}}$ the prediction provided by the OLS regression. Upon examining Fig. 9(a), it is evident that F_x is linearly dependent on V_{max}. With $R^2 = 0.90$, the data shows minimal scatter, indicating that most of the variation in F_x can be attributed to changes in V_{max}. Notably, V_{max} provides a better fit to the data than the conventionally adopted crest height elevations, η_c or $\Delta\eta$ (see Fig. 1). This suggests that the overall wave shape, in addition to the level of inundation, $\Delta\eta$, plays a critical role in determining the magnitude of WID loading.

The strong dependence of F_x on V_{max} can be explained by two factors. First, the sea-state (SS1) does not include a large amount of breaking waves, and second, the spatial evolution of waves in a random sea is more varied. Both factors reduce, on average, the likelihood of impulsive loads occurring, as these require a breaking wave impacting near the front-centre of the topside structure. However, it is important to note that the worst-case F_x remains governed by impulsive loading caused by breaking waves. In such cases, the significance of u_{max} increases while that of V_{max} drops, as highlighted in previous studies. Indeed, as shown in Fig. 9(b), when considering the steepest sea-state in the dataset (SS5) where wave breaking is more prominent, R^2 reduces to 0.83, indicating a weaker dependence on V_{max} under these conditions. It is noted that the p-values of both OLS fits are less than 1×10^{-4}. The observed pattern is consistent for all the sea-states involved in this study.

5.3. The effect of water particle kinematics

Within Eq. (13) the residual, $\epsilon = F_x - \hat{F}_x$, represents the remaining variation in F_x after isolating the influence of V_{max}. Fig. 10 investigates the correlation of this residual with Grue et al.'s (2003) estimate of the maximum horizontal water particle velocities, $\hat{u}_{max}$. This was calculated using the crest elevation and $\bar{f}$ measured at WG25 in sea-state SS1. In sub-plot (a) the residual is positively correlated to $\hat{u}^2_{max}$ with $R^2 = 0.14$.[1] In other words, waves with larger $\hat{u}_{max}$ are expected to be associated with larger F_x, assuming constant V_{max}. Interestingly, when considering a steeper sea-state, SS5, R^2 increases to a value of 0.27, signifying a much larger dependence of F_x on the velocities due to an increase in the occurrence of breaking waves.

It should be noted that within this figure, sub-plot (a) contains loading data caused by those incident waves reaching their maximum crest elevation before propagating to the centre of the structure (i.e. η_c^A observed upstream of WG25). In contrast, sub-plot (b) contains data associated with incident waves where η_c^A was attained downstream of WG25. In this latter case $R^2 = 0$ at a significance level of 1%.

Whilst the p-value for the OLS regression in sub-plot (a) is less than 1×10^{-4}, it is equal to 0.282 in sub-plot (b).

The explanation for this difference lies in the behaviour of the underlying wave frequency components. When these components focus to attain η_c^A (and the underlying velocities approaching u_{max}) at the front half of the topside structure, they tend to 'phase lock' (Gibson and Swan, 2007) and remain focused as they propagate through the rest of the structure. In this case the actual velocities arising during the loading process are more accurately and persistently represented by $\hat{u}_{max}$, resulting in a stronger correlation between F_x and $\hat{u}^2_{max}$. The relationship between these variables is again consistent for all the sea-states in Table 1.

In performing the above analysis, it should be noted that u_{max} is generally not entirely independent of V_{max}. However, the dependence appears to be weaker in random seas compared to QD focused waves. Evidence of this is provided in Fig. 11, which plots V_{max} against $\hat{u}_{max}$ for a set of wave events in SS1. For comparison, the same data for QD focused waves are also included. In order to facilitate a more direct comparison, in both cases the wave events have very similar η_c^A, where $15.5\,m \le \eta_c^A \le 16.5\,m$. With η_c^A being held close to each other, smaller V_{max} typically corresponds to a steeper wave profile. For the QD focused waves, this reduced steepness results in an expected increase in $\hat{u}_{max}$. In contrast, the random wave data (black dots) show little correlation between these two quantities. This difference can be explained by the fact that QD waves are generated along the centre-line of the topside structure ($y = 0\,m$) and are designed to ensure the maximum crest elevation (η_c^A) occurs within the structure's footprint. Under these conditions, u_{max} almost always occurs during the wave-structure interaction. In contrast, for random waves, this occurs less consistently, leading to weaker correlation between V_{max} and u_{max}.

Taken together, the above observations provide further explanation for the identified key parameters listed in Table 3. In random seas, while F_x remains primarily dependent on the incident wave momentum, represented by V_{max} and u_{max}, the variability of incident wave forms leads to more diverse loading conditions compared to QD focused waves. As a result, additional parameters are necessary to accurately determine the applied loading. These include η_c measured at multiple locations to capture spatial variations and Q to account for the temporal persistence of the maximum crest and velocities. Furthermore, since u_{max} is dependent on both η_c and $\bar{f}$ as expressed in Eq. (8), $\bar{f}$ becomes critical as it provides the remaining missing information required to characterise the kinematics.

[1] $\hat{u}^2_{max}$ is adopted in this linear regression since force is typically linearly related to velocity squared.

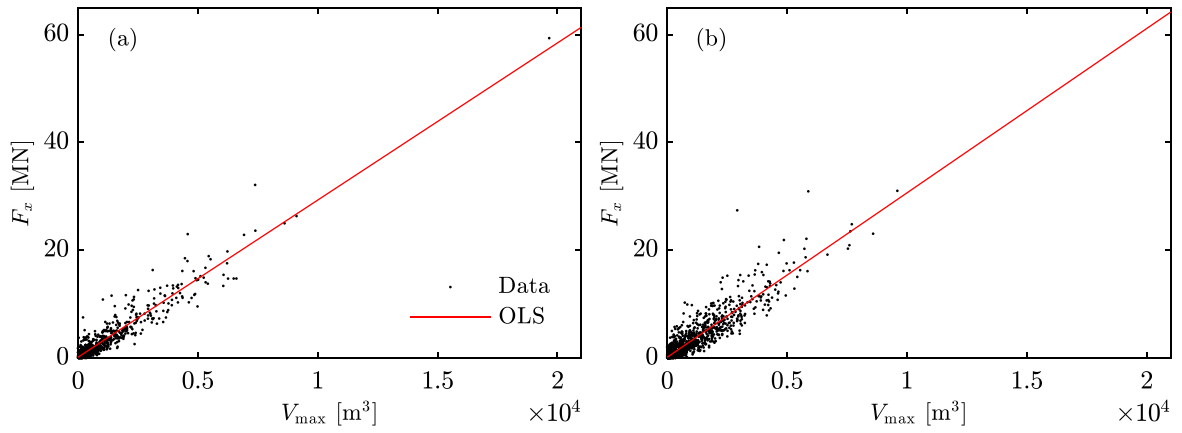


Fig. 9. Correlation between $V_{\max}$ and F_x arising in (a) SS1 and (b) SS5. The correlation is assessed using an Ordinary Least-Square (OLS) fit.

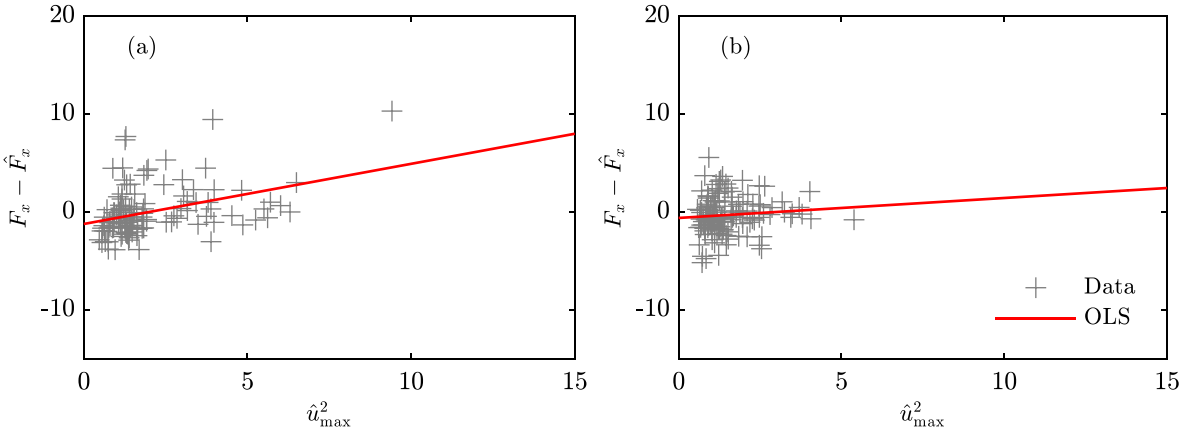


Fig. 10. Scatter plots of $\epsilon = F_x - \hat{F}_x$ and $\hat{u}^2_{max}$; the latter evaluated using the free-field water surface elevation measured at WG25 in SS1. (a) Data corresponding to waves reach their maximum η_c^A upstream and (b) downstream of WG25.

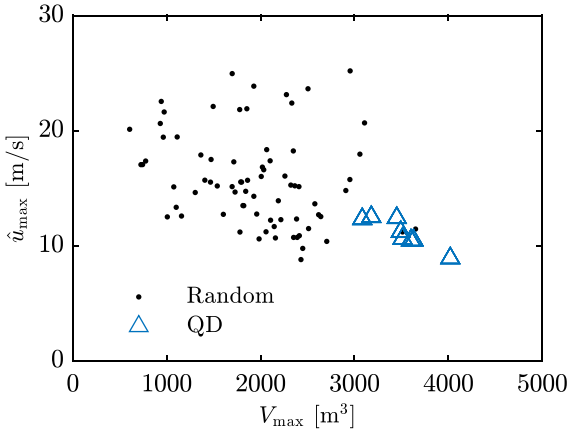


Fig. 11. A comparison between random and QD focused waves in terms the relationship between $V_{\max}$ and $\hat{u}_{\max}$. The presented wave events are selected from Fig. 1(a) where $15.5\,\text{m} \le \eta_c^A \le 16.5\,\text{m}$.

5.4. Variation of sea-state parameters

The present section evaluates the variation in the mean F_x as the sea-state changes. This is important because, in practice, the annual probability of failure is jointly influenced by all possible sea-states that may occur at the structure. Based on earlier discussions, the focus will be on two key parameters, $V_{\max}$ and $\bar{f}$, and their variation with the sea-state parameters. Fig. 12 presents the QQ-plots as the sea-state parameters vary, whereas Fig. 13 provides the corresponding changes in $V_{\max}$, $\bar{f}$ and F_x; the quantities being averaged for the loading events associated with $15.5\,\text{m} \le \eta_c^A \le 16.5\,\text{m}$. Taking each pair of sub-plots in these two figures in turn:

(a) With all other parameters held constant and varying the directional spreading, σ_θ, F_x appears to reduce with increasing σ_θ for a given level of inundation. This is entirely consistent with expectations, as increased directionality leads to reduced $V_{\max}$ and $u_{\max}$; both due to the more short-crested nature of the incident waves. This is confirmed in Fig. 13(a), showing that both $V_{\max}$ and $\bar{f}$ (which is positively correlated with $u_{\max}$) decrease, leading to a corresponding reduction in F_x. It is also interesting to note that the loading variability reduces with increasing directional spreading. This reflects a smaller variation in the incident wave form due to a reduced nonlinear wave-wave interaction when the wave becomes more short-crested (Latheef et al., 2017).

(b) Increasing H_s (while keeping all other parameters constant) has a small but measurable effect on the applied WID loading. The two sea-states (SS1 and SS5) in Fig. 12(b) have $H_s = 15\,\text{m}$ and $H_s = 17.5\,\text{m}$, respectively. It was observed that the sea-state with lower H_s yields F_x larger by up to 10%, particularly for $\eta_c^A \ge 15\,\text{m}$. This is consistent with the observations in Fig. 13(b), where the sea-state with lower H_s produces larger $\bar{f}$, leading to a larger F_x for a given η_c^A. At the same time the changes in $V_{\max}$ are minimal. This behaviour is explained by the fact that for a

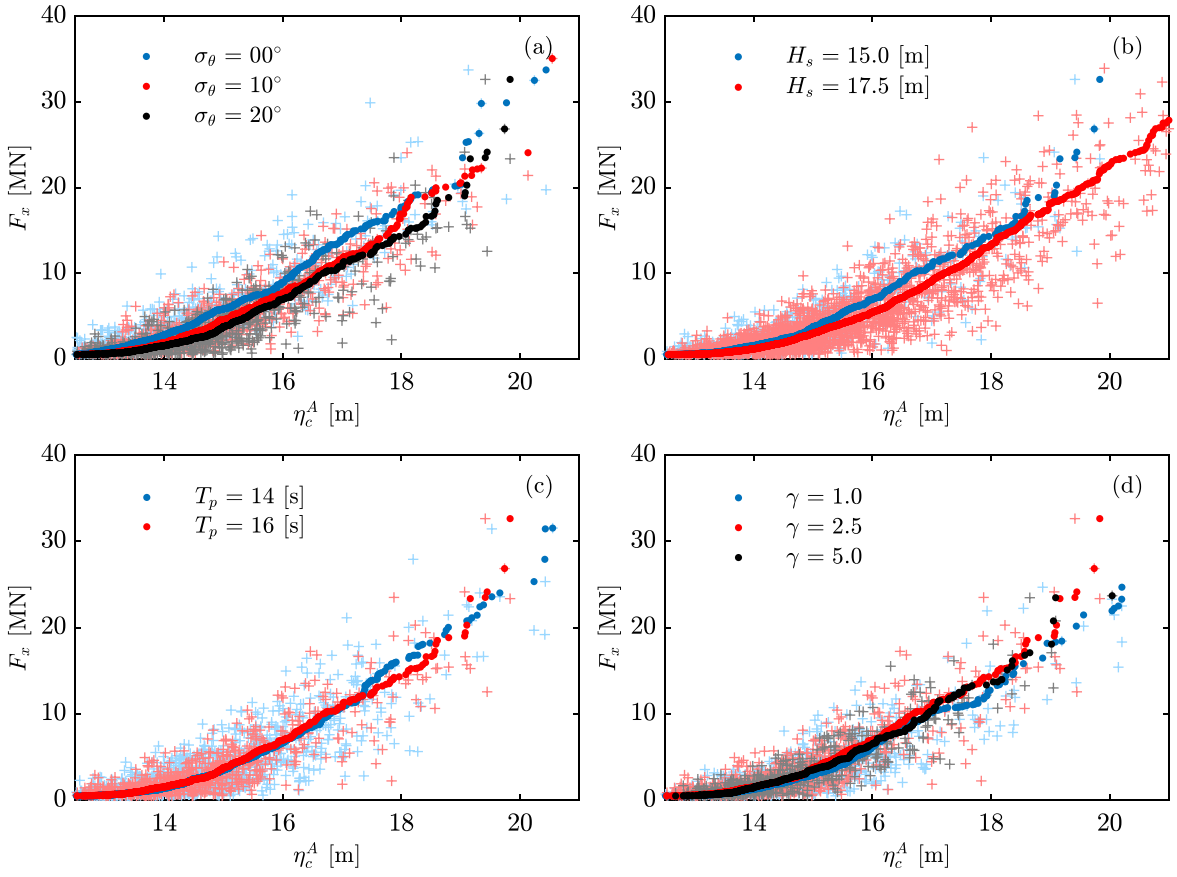


Fig. 12. QQ-plots showing the influence of sea-state parameters (σ_θ, H_s, T_p, γ) on the applied WID loading.

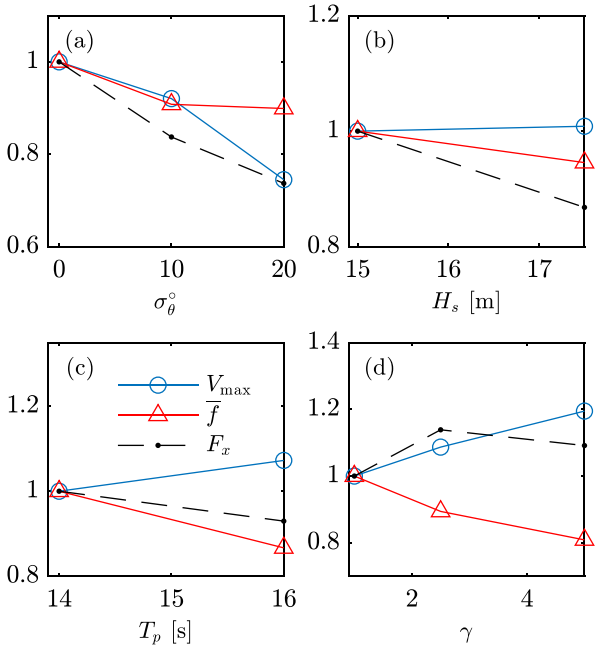


Fig. 13. Changes in the $V_{\max}$, $\bar{f}$ and F_x with varying sea-state parameters (σ_θ, H_s, T_p, γ), averaged for the loading events associated with $15.5\,\text{m} \le \eta_c^A \le 16.5\,\text{m}$.

similar level of inundation, the sea-state with lower H_s consists of steeper individual waves that are subject to stronger nonlinear wave-wave interactions. In contrast, waves of equivalent η_c^A in SS8 have likely already undergone significant wave breaking before loading the topside structure, leading to a reduction in the overall wave steepness and the associated velocities.

(c) Figs. 12(c) and 13(c) examine a similar set of comparisons related to variations with T_p, suggesting minimal, if any, differences. While this might seem surprising, as a smaller T_p typically results in steeper waves and thus larger $u_{\max}$, there may be a degree of cancellation with $V_{\max}$, which decreases as steepness increases. Fig. 13(c) clearly illustrates this point.

(d) The peak enhancement factor, γ, does not appear to have a significant effect on F_x. As γ increases, the energy associated with high-frequency wave components decreases, causing the underlying wave spectrum to become more narrow-banded. This reduces the rate of wave evolution, allowing both $V_{\max}$ and $u_{\max}$ to remain more persistent as the wave propagates through the structure. However, the reduction in high-frequency energy also reduces the likelihood of nonlinear wave-wave interactions, which act to reduce the velocities. These opposing effects result in a degree of cancellation, as confirmed in Fig. 13(d).

Taken together, these observations further confirm that the characteristics of WID loading events depend on the properties of individual waves rather than the overall sea-state characteristics.

6. WID load predictions using the new data-driven model

Given the physical insights discussed above, it is clear that the applied WID loading can be entirely described by the incident wave properties. To further demonstrate this point, a final ANN model is trained on the topside model as given in Fig. 3. The dataset used for training comprises 700 randomly selected WID events from SS1, which

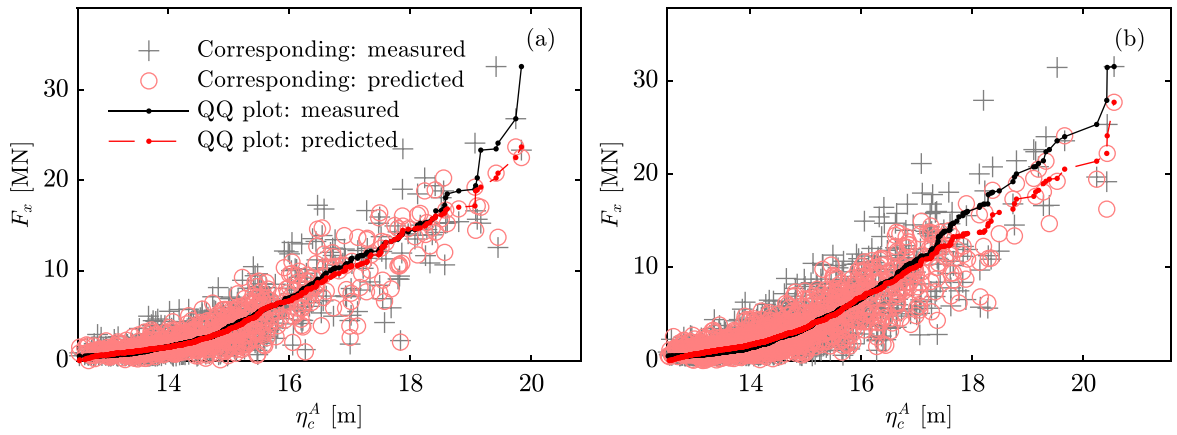


Fig. 14. A comparison between the measured (true) F_x and the predicted values. The dataset is collected in (a) sea-state SS1 and (b) SS5. None of the data is used as part of the training dataset.

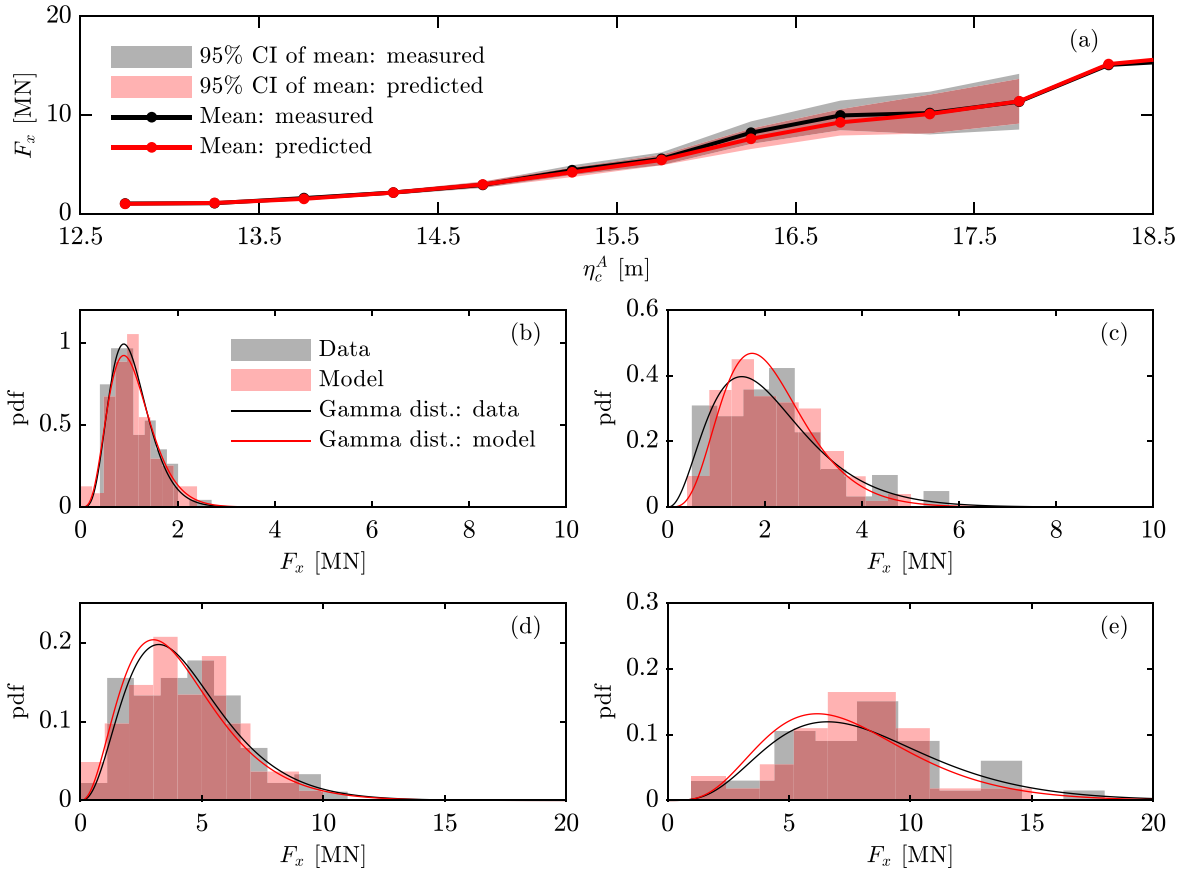


Fig. 15. A comparison between the measured and the predicted uncertainties in F_x for different levels of η_c^A. Sub-plot (a) presents the mean and its 95% confidence interval for F_x values at different levels of η_c^A. Sub-plots (b)-(e) present the histograms and the fitted Gamma distributions in individual η_c^A bins: $\eta_c^A \in$ [13.0, 13.5], [14.0, 14.5], [15.0, 15.5] and [16.0, 16.5] m. The data presented relate to SS1.

is only a part of the data measured for SS1. No measure is required to prevent overfitting during training.

The accuracy of the model is then tested against experimental data completely independent of the training set, generated for the test cases given in Table 1. The comparisons that follow verify the predictive capabilities of the proposed model and its capacity to capture the uncertainty of WID loading in random seas.

Fig. 14(a) and (b) compare the measured and predicted maximum WID loads, F_x, for two different sea-states, SS1 and SS5, respectively. From this figure it is clear that the predicted QQ-plots are in great agreement with the experimental measurements. In reviewing this result, it should be noted that Fig. 14(b) corresponds to a very steep sea-state, with a considerably higher number of breaking waves and instances of low-probability events. This makes it one of the most challenging cases to compare against for the reasons discussed in Section 5. Despite this, in both cases the agreement is remarkable for realistic levels of deck inundation, approximately $\eta_c \leq 15.5$ m. For $\eta_c \geq 17.5$ m, the number of data points and the associated scatter means that it is difficult to infer statistically significant results. Indeed, most discrepancies arising from the predictions are generally within the range of the aleatoric statistical uncertainty and typical for WID measurements and predictions.

Table 4
The RMSE between measured and predicted F_x for both the corresponding data and the QQ-plots. The predictions made using a model trained using separate data related to SS1 only.

ID	SS1	SS2	SS3	SS4	SS5	SS6	SS7	SS8
RMSE [MN]	1.19	0.87	1.07	1.33	1.43	1.44	1.65	1.67
RMSE-QQ [MN]	0.51	0.32	0.47	0.50	0.60	0.39	0.70	0.59

In order to quantify the success of applying the trained ANN model to sea-states other than SS1 and SS5, Table 4 summarises RMSE between the predicted and measured F_x for all sea-states in Table 1. The error is calculated for both the corresponding data and the QQ-plots. In considering the metrics in Table 4, it is important to note that the same ANN model is used as in Fig. 14 to predict loading arising in new sea-states without retraining. It is clear that the prediction accuracy of the model remains relatively constant when applied to unseen WID events that arise in different sea-states.

Fig. 15 provides a more detailed assessment, through the ANN model predictions, on how well the variability of the WID loads is captured by the variations in the incident wave properties. To produce this figure, the predicted and measured 'corresponding' loads from Fig. 14 are binned according to η_c^A values. The mean F_x and its 95% confidence interval (CI) for each bin are computed and plotted in Fig. 15(a). It should be noted that for the highest crest elevations ($\eta_c^A > 17.75$ m), corresponding to the rarest events, there were insufficient data to reliably compute the CI. Therefore, data in this region were excluded from the analysis. Nevertheless, the CI at all other levels of inundation is well described by the predictions, which rely solely on incident wave parameters as inputs. It is clear that the model predictions are almost identical to the measurements and their confidence intervals overlapping.

It should be noted that a similar level of prediction accuracy is achieved for all other sea-states involved in this study.

Finally, Figs. 15(b)-(e) present histograms and fitted Gamma distributions of F_x for several η_c^A ranges (bins) which, effectively, provide the conditional probability distribution $P(F_x|\eta_c^A)$. In all four sub-plots, the predicted distributions are in excellent agreement with the experimental measurements. Importantly, this information is critical for determining the probability of exceedance of a given WID load, a key input for full reliability analyses of offshore structures. Taken together, the proposed ANN architecture using the parameters listed in Table 3 provides a promising, highly efficient tool for the prediction of WID loading, which will be provided as a companion to the present paper.

7. Conclusions

When subjected to random waves, wave-in-deck (WID) loading on offshore topside structures exhibits a significant increase in variability. Existing studies using quasi-deterministic focused waves, despite incorporating a wide range of incident wave properties, have not provided a satisfactory explanation for this phenomenon. The present study addresses this issue through new experiments conducted across a broad range of random sea-states, measuring both the full incident wave profiles and the applied WID loading (F_x). Increased variability in WID loading was observed in all sea-states investigated.

Using a data-driven approach, the measurements were systematically analysed on a wave-by-wave basis with an ANN model. From a wide set of candidate parameters based on the free-field incident wave properties, strong correlations were identified between F_x and key parameters such as the maximum volume of water entering the deck structure ($V_{\max}$) and the maximum water particle kinematics ($u_{\max}$). While these findings confirm that the loading process remains momentum-driven in random seas, $V_{\max}$ has been found to play an increased role. New parameters related to the spatial and temporal variations of the incident wave were also identified to heavily influence the applied WID loading. These include wave properties measured at multiple locations, capturing spatial variability, and the focal quality of the incident wave crest, capturing temporal variability. Crucially, it is this increased variation in the evolution of individual incident waves that drives the observed increase in WID loading variability in random seas. Unlike experiments conducted in QD focused waves, for a given incident wave event in a random sea the structure is not always loaded by the maximum crest elevation. Indeed, rather than sea-state-wide parameters, it is the properties of individual waves that determine the magnitude of WID loading, underscoring the importance of adopting random seas as design conditions in full reliability assessments if randomness is to be adequately incorporated.

These findings were further validated by comparing the predictions of the trained ANN model on a completely independent dataset for the same structure. It was shown that WID loads are very well described by the new model. This was achieved not only for the mean F_x at given levels of inundation but also for the variability of loading around the mean. As a whole, the present method has been shown to be efficient, capable of producing accurate predictions to a wide range of sea-states even when trained on a small dataset. As such, the application of ANN models in WID prediction emerge as useful tools to supplement existing methods in reliability assessments.

CRediT authorship contribution statement

Chong Huo: Writing – review & editing, Writing – original draft, Visualization, Investigation, Formal analysis. **Li Ma:** Writing – review & editing, Supervision, Conceptualization. **Ioannis Karmpadakis:** Writing – review & editing, Supervision, Conceptualization.

Declaration of competing interest

The authors declare that they have no known competing financial interests or personal relationships that could have appeared to influence the work reported in this paper.

References

Adcock, T.A.A., Gibbs, R.H., Taylor, P.H., 2012. The nonlinear evolution and approximate scaling of directionally spread wave groups on deep water. Proc. R. Soc. A 468, 2704–2721. http://dx.doi.org/10.1098/rspa.2012.0029, URL: https://royalsocietypublishing.org/.

Alberello, A., Chabchoub, A., Monty, J.P., Nelli, F., Lee, J.H., Elsnab, J., Toffoli, A., 2018. An experimental comparison of velocities underneath focussed breaking waves. Ocean Eng. 155, 201–210. http://dx.doi.org/10.1016/j.oceaneng.2018.02.049, URL: https://www.sciencedirect.com/science/article/pii/S0029801818301987.

API, 2014. Structural integrity management of fixed offshore structures api rp 2sim.

Arena, F., Ascanelli, A., Nava, V., Pavone, D., Romolo, A., 2008. Three-dimensional nonlinear random wave groups in intermediate water depth. Coast. Eng. 55, 1052–1061. http://dx.doi.org/10.1016/j.coastaleng.2008.04.002, URL: https://linkinghub.elsevier.com/retrieve/pii/S0378383908000823.

Baldock, T.E., Swan, C., Taylor, P.H., 1996. A laboratory study of nonlinear surface waves on water. Philos. Trans. R. Soc. A: Math. Phys. Eng. Sci. 354, 650–675. http://dx.doi.org/10.1098/rsta.1996.0022.

Bishop, C.M., 1995. Neural Networks for Pattern Recognition. Oxford University Press.

Boccotti, P., 1989. On Mechanics of Irregular Gravity Waves. Accademia Nazionale dei Lincei.

Chuang, W.L., Lin, T.C., Wang, Y.J., 2023. Greenwater due to plunging breaking wave impingement on a deck structure, part 1: Experimental investigation on fluid kinematics. Ocean Eng. 287, 115859. http://dx.doi.org/10.1016/J.OCEANENG.2023.115859.

DNV-GL, 2019. Recommended Practice DNVGL-RP-C205: Environmental Conditions and Environmental Loads. DNV-GL.

Donelan, M.A., Drennan, W.M., Magnusson, A.K., 1996. Nonstationary analysis of the directional properties of propagating waves. J. Phys. Oceanogr. 26, 1901–1914. http://dx.doi.org/10.1175/1520-0485(1996)026<1901:NAOTDP>2.0.CO;2.

Duong, T.T., Jung, K.H., Lee, G.N., Suh, S.B., 2024. Physics-informed neural network for the reconstruction of velocity and pressure of wave-in-deck loading from particle image velocimetry data. Appl. Ocean Res. 153, 104193. http://dx.doi.org/10.1016/J.APOR.2024.104193.

Fei, L., Fang, Q., Liu, J., Guo, A., 2024. Investigation into the relationship between wave forces and characteristic velocity during wave impact on the deck structures. Ocean Eng. 309, 118403. http://dx.doi.org/10.1016/J.OCEANENG.2024.118403.

Forristall, G.Z., 2000. Wave crest distributions: Observations and second-order theory. J. Phys. Oceanogr. 30, 1931–1943. http://dx.doi.org/10.1175/1520-0485(2000)030<1931:WCDOAS>2.0.CO;2.

Forristall, G.Z., 2008. How should we combine long and short term wave height distributions? In: Structures, Safety and Reliability, vol. 2, ASMEDC, pp. 987–994. http://dx.doi.org/10.1115/OMAE2008-58012, URL: https://asmedigitalcollection.asme.org/OMAE/proceedings/OMAE2008/48197/987/331183.

Gibbs, R.H., Taylor, P.H., 2005. Formation of walls of water in 'fully' nonlinear simulations. Appl. Ocean Res. 27, 142–157. http://dx.doi.org/10.1016/j.apor.2005.11.009.

Gibson, R.S., Swan, C., 2007. The evolution of large ocean waves: The role of local and rapid spectral changes. Proc. R. Soc. A: Math. Phys. Eng. Sci. 463, 21–48. http://dx.doi.org/10.1098/rspa.2006.1729.

Grue, J., Clamond, D., Huseby, M., Jensen, A., 2003. Kinematics of extreme waves in deep water. Appl. Ocean Res. 25, 355–366. http://dx.doi.org/10.1016/j.apor.2004.03.001, URL: https://www.sciencedirect.com/science/article/pii/S0141118704000264.

Guedes Soares, C., Cherneva, Z., Antão, E., 2004. Steepness and asymmetry of the largest waves in storm sea states. Ocean Eng. 31, 1147–1167. http://dx.doi.org/10.1016/j.oceaneng.2003.10.014, URL: https://linkinghub.elsevier.com/retrieve/pii/S0029801804000113.

Guyon, I., Elisseeff, A., 2003. An introduction to variable and feature selection. J. Mach. Learn. Res. 3, 1157–1182. http://dx.doi.org/10.1162/153244303322753616.

Hague, C.H., Swan, C., 2009. A multiple flux boundary element method applied to the description of surface water waves. J. Comput. Phys. 228, http://dx.doi.org/10.1016/j.jcp.2009.04.012.

Hasselmann, K., Barnett, T.P., Bouws, E., Carlson, H., Cartwright, D.E., Enke, K., Ewing, J.A., Gienapp, H., Hasselmann, D.E., Kruseman, P., Meerburg, A., Muller, P., Olbers, D.J., Richter, K., Sell, W., Walden, H., 1973. Measurements of wind-wave growth and swell decay during the joint north sea wave project (jonswap). Coast. Eng. 7, 399–404.

Hastie, T., Tibshirani, R., Friedman, J., 2009. The Elements of Statistical Learning. Springer New York, http://dx.doi.org/10.1007/978-0-387-84858-7.

Heidman, J., Weaver, T., 1992. Static wave loading procedure for platform design. Civ. Eng. Ocean. V 496–519.

Holthuijsen, L.H., 2007. Waves in Oceanic and Coastal Waters. Cambridge University Press, http://dx.doi.org/10.1017/CBO9780511618536.

Hornik, K., Stinchcombe, M., White, H., 1989. Multilayer feedforward networks are universal approximators. Neural Netw. 2, 359–366. http://dx.doi.org/10.1016/0893-6080(89)90020-8.

Johannessen, T.B., Swan, C., 2003. On the nonlinear dynamics of wave groups produced by the focusing of surface-water waves. Proc. R. Soc. A: Math. Phys. Eng. Sci. 459, 1021–1052. http://dx.doi.org/10.1098/rspa.2002.1028.

Karmpadakis, I., 2019. Wave Statistics in Intermediate and Shallow Water Depths. (Ph.D. thesis). Imperial College London.

Karmpadakis, I., Swan, C., 2020. On the average shape of the largest waves in finite water depths. J. Phys. Oceanogr. 50, 1023–1043. http://dx.doi.org/10.1175/JPO-D-19-0165.1.

Karmpadakis, I., Swan, C., 2022. A new crest height distribution for nonlinear and breaking waves in varying water depths. Ocean Eng. 266, http://dx.doi.org/10.1016/j.oceaneng.2022.112972.

Karmpadakis, I., Swan, C., Christou, M., 2019. Laboratory investigation of crest height statistics in intermediate water depths. Proc. R. Soc. A: Math. Phys. Eng. Sci. 475, http://dx.doi.org/10.1098/rspa.2019.0183.

Karmpadakis, I., Swan, C., Christou, M., 2020. Assessment of wave height distributions using an extensive field database. Coast. Eng. 157, 103630. http://dx.doi.org/10.1016/j.coastaleng.2019.103630.

Karmpadakis, I., Swan, C., Christou, M., 2022. A new wave height distribution for intermediate and shallow water depths. Coast. Eng. 175, 104130. http://dx.doi.org/10.1016/j.coastaleng.2022.104130.

Krogstad, H.K., Magnusson, A.K., Donelan, M.A., 2006. Wavelet and local directional analysis of ocean waves. In: Proceedings of the International Offshore and Polar Engineering Conference, vol. 16, pp. 66–73.

Latheef, M., Swan, C., 2013. A laboratory study of wave crest statistics and the role of directional spreading. Proc. R. Soc. A: Math. Phys. Eng. Sci. 469, http://dx.doi.org/10.1098/rspa.2012.0696.

Latheef, M., Swan, C., Spinneken, J., 2017. A laboratory study of nonlinear changes in the directionality of extreme seas. Proc. R. Soc. A: Math. Phys. Eng. Sci. 473, http://dx.doi.org/10.1098/rspa.2016.0290.

Lindgren, G., 1970. Some properties of a normal process near a local maximum. Ann. Math. Stat. 41, 1870–1883. http://dx.doi.org/10.1214/aoms/1177696688.

Lindgren, G., Prevosto, M., 2021. The relation between wave asymmetry and particle orbits analysed by slepian models. J. Fluid Mech. 924, 1–27. http://dx.doi.org/10.1017/jfm.2021.607.

Ma, L., 2017. The Effective Modelling of Wave-in-Deck Loads (Ph.D. thesis). Imperial College London.

Ma, Y., Dong, G., Ma, X., Wang, G., 2010. A new method for separation of 2d incident and reflected waves by the Morlet wavelet transform. Coast. Eng. 57, 597–603. http://dx.doi.org/10.1016/j.coastaleng.2010.01.002, URL: http://dx.doi.org/10.1016/j.coastaleng.2010.01.002.

Ma, L., Swan, C., 2020a. An experimental study of wave-in-deck loading and its dependence on the properties of the incident waves. J. Fluids Struct. 92, http://dx.doi.org/10.1016/j.jfluidstructs.2019.102784.

Ma, L., Swan, C., 2020b. The effective prediction of wave-in-deck loads. J. Fluids Struct. 95, http://dx.doi.org/10.1016/j.jfluidstructs.2020.102987.

Ma, L., Swan, C., 2023a. An experimental study of wave-in-deck loading and its dependence on the properties of the topside structure. Mar. Struct. 88, 103340. http://dx.doi.org/10.1016/J.MARSTRUC.2022.103340.

Ma, L., Swan, C., 2023b. Wave-in-deck loads: an assessment of present design practice given recent improvements in the description of extreme waves and the nature of the applied loads. Ocean Eng. 285, 115302. http://dx.doi.org/10.1016/j.oceaneng.2023.115302.

Masterton, S.R., Swan, C., 2008. On the accurate and efficient calibration of a 3d wave basin. Ocean Eng. 35, 763–773. http://dx.doi.org/10.1016/J.OCEANENG.2008.02.002.

McAllister, M.L., Draycott, S., Adcock, T.A.A., Taylor, P.H., Van Den Bremer, T.S., 2018. Laboratory recreation of the Draupner wave and the role of breaking in crossing seas. J. Fluid Mech. 860, 767–786. http://dx.doi.org/10.1017/jfm.2018.886.

Millar, O., Ma, L., Karmpadakis, I., 2025. Tsunami-induced loads on coastal structures: Experimental investigation and prediction. Ocean Eng. 336, http://dx.doi.org/10.1016/j.oceaneng.2025.121762.

Nocedal, J., Wright, S.J., 2006. Numerical Optimization, second ed. Springer New York, http://dx.doi.org/10.1007/978-0-387-40065-5.

Phillips, O.M., Gu, D., Donelan, M., 1993. Expected structure of extreme waves in a Gaussian sea. part i: Theory and swade buoy measurements. J. Phys. Oceanogr. 992–1000.

Powers, E.J., Yi, E.J., Park, I.S., Chung, J.H., 1998. Wavelet-based bicoherence analysis of irregular wave data. In: Proceedings of the International Offshore and Polar Engineering Conference, vol. 3, pp. 170–175.

Seiffert, B.R., Ducrozet, G., 2018. Simulation of breaking waves using the high-order spectral method with laboratory experiments: wave-breaking energy dissipation. Ocean. Dyn. 68, 65–89. http://dx.doi.org/10.1007/s10236-017-1119-3, URL: http://link.springer.com/10.1007/s10236-017-1119-3.

Shannon, C.E., 1948. A mathematical theory of communication. Bell Syst. Tech. J. 27, 379–423. http://dx.doi.org/10.1002/j.1538-7305.1948.tb01338.x.

Sharma, J., Dean, R., 1981. Second-order directional seas and associated wave forces. Soc. Pet. Eng. 4, 129–140.

Spinneken, J., Swan, C., 2009a. Second-order wave maker theory using force-feedback control, part i: A new theory for regular wave generation. Ocean Eng. 36, 539–548. http://dx.doi.org/10.1016/j.oceaneng.2009.01.019.

Spinneken, J., Swan, C., 2009b. Second-order wave maker theory using force-feedback control, part ii: An experimental verification of regular wave generation. Ocean Eng. 36, 549–555. http://dx.doi.org/10.1016/j.oceaneng.2009.01.007.

Stansberg, C., 2020. Wave front steepness and influence on horizontal deck impact loads. J. Mar. Sci. Eng. 8 (314), http://dx.doi.org/10.3390/jmse8050314.

Stockwell, R.G., Mansinha, L., Lowe, R.P., 1996. Localization of the complex spectrum: The s transform. IEEE Trans. Signal Process. 44, 998–1001. http://dx.doi.org/10.1109/78.492555.

Tayfun, M.A., 1981. Distribution of crest-to-trough wave heights. J. Waterw. Port Coast. Ocean. Eng. http://dx.doi.org/10.1061/JWPCDX.0000259.

Tayfun, M., Fedele, F., 2007. Expected shape of extreme waves in storm seas. In: Proceedings of the International Conference on Offshore Mechanics and Arctic Engineering. OMAE, pp. 53–60.

Toffoli, A., Alberello, A., Clarke, H., Nelli, F., Benetazzo, A., Bergamasco, F., Ntamba, B.N., Vichi, M., Onorato, M., 2024. Observations of rogue seas in the southern ocean. Phys. Rev. Lett. 132, 154101. http://dx.doi.org/10.1103/PhysRevLett.132.154101, URL: https://link.aps.org/doi/10.1103/PhysRevLett.132.154101.

Tromans, P., Anaturk, A., Hagemeijer, P., 1991. A new model for the kinematics of large ocean wave-application as a design wave. In: In the First International Conference on Ocean, Offshore and Arctic Engineering. American Society of Mechanical Engineers.

Wang, H., Santo, H., Taylor, P.H., Dai, S.S., Day, A.H., Chan, E.S., 2022. Wave impacts on a solid deck in transient wave groups. J. Fluids Struct. 114, 103755. http://dx.doi.org/10.1016/J.JFLUIDSTRUCTS.2022.103755.

Wu, Y.T., Chang, K.A., 2024. Experimental study on flow kinematics of breaking wave impinging and overtopping on a deck structure. Ocean Eng. 302, 117663. http://dx.doi.org/10.1016/J.OCEANENG.2024.117663.

Zhou, T., Ma, Z., Zhai, G., Chen, J., 2023. Wave-in-deck loads induced by regular wave impact: The role of compressible air entrainment. J. Fluids Struct. 122, 103974. http://dx.doi.org/10.1016/J.JFLUIDSTRUCTS.2023.103974.